JOURNAL OF PROPULSION AND POWER
Vol. 24, No. 5, September–October 2008

Performance Modeling of a Coaxial Radio-Frequency Gas-Discharge Microthruster

William B. Stein,* Alina A. Alexeenko,† and Ivana Hrbud‡
Purdue University, West Lafayette, Indiana 49707

DOI: 10.2514/1.34036

A method to model the radio-frequency gas-discharge microthruster performance using particle-in-cell, Monte Carlo collisions, and direct simulation Monte Carlo methods is presented. The radio-frequency gas-discharge microthruster is an electrothermal device that exploits a capacitively coupled discharge to heat a propellant. The plasma is characterized as a highly uniform, low-current density discharge propagating through a low-pressure gas. To computationally assess the thruster's propulsive capabilities, a numerical model composed of particle-in-cell/Monte Carlo collisions and direct simulation Monte Carlo algorithms is used. A gas heat transfer model is included to enhance the particle-in-cell/Monte Carlo collision simulations and to reflect the effects of neutral gas heating by the plasma. The effects of inner electrode radius (0.5–10 mm), applied voltage (10–500 V), applied frequency (200–1000 MHz), and pressure (0.1–10 torr) on thruster performance are investigated. Particle-in-cell/Monte Carlo collision simulations are used to determine the overall trends in plasma characteristics within this parameter space. These simulations show that increases in discharge pressure, radio frequency, applied potential, and inner radius transmit more power into the fluid. However, the efficiency of power transmission into the fluid increases with a decrease in either inner electrode radius or radio frequency and increases with applied voltage and pressure. Heat transfer within the plasma discharge was shown to greatly affect the discharge characteristics and thruster performance. Increasing the neutral temperature reduces the neutral density, thus reducing the power-transmission efficiency. Thrust calculations using the direct simulation Monte Carlo method demonstrate that the coaxial radio-frequency gas-discharge microthruster achieves a specific impulse in excess of 30% greater than a cold-gas expansion.

Nomenclature

A_{surf}	=	electrode surface area, m^{-2}
A^*	=	sonic area, m^2
C_p	=	specific heat at constant pressure, $\text{J kg}^{-1}\ \text{K}^{-1}$
d_{gap}	=	electrode separation distance, m
$\mathbf{E}$	=	electric field, V m^{-1}
e	=	electron charge, C
F	=	thrust, mN
f	=	number density distribution function
g	=	gravitational constant, ms^{-1}
I_{sp}	=	specific impulse, s
J_1	=	fundamental current density through a sheath, Am^{-2}
j	=	current density, Am^{-2}
k	=	thermal conductivity, $\text{W m}^{-1}\ \text{K}^{-1}$
L_{ch}	=	discharge chamber length, m
m	=	neutral particle mass, kg
$\dot{m}$	=	mass flux, mgs^{-s}
m_e	=	electron mass, kg
n	=	neutral gas number density, m^{-3}
n_e	=	electron number density, m^{-3}
n_i	=	ion number density, m^{-3}
n_o	=	electron number density of the discharge center, m^{-3}
n_s	=	electron number density of the sheath edge, m^{-3}
nc	=	number of computational cells
$nc2p$	=	ratio of computational to physical particles
P	=	pressure, torr
$\mathbb{P}_{\text{abs}}$	=	absorbed power, W
$\mathbb{P}_f$	=	power transmitted into the fluid, W
$\mathbb{P}_W$	=	power loss to walls, W
$\mathbb{P}_C^{\text{cx}}$	=	power loss to charge-exchange collisions, W
$\mathbb{P}_C^{\text{el}}$	=	power loss to elastic collisions, W
$\mathbb{P}_C^{\text{ex}}$	=	power loss to excitation collisions, W
$\mathbb{P}_C^{\text{in}}$	=	power loss to ionization collision, W
P_0	=	stagnation pressure, Pa
R	=	gas constant, $\text{J K}^{-1}\ \text{kg}^{-1}$
R_{orf}	=	orifice radius, mm
r	=	radius, mm
r_0	=	inner radius, mm
r_1	=	outer radius, mm
$\bar{S}_{\text{ohm}}$	=	ohmic heating per unit area, W m^{-2}
$\bar{S}_{\text{stoch}}$	=	stochastic heating per unit area, W m^{-2}
T	=	temperature, K
T_{de}	=	temperature at discharge exit, K
$\bar{T}_e$	=	electron temperature, eV
$\bar{T}_{\text{gas}}$	=	volume averaged neutral temperature, K
T_{ref}	=	reference temperature (273.2 K)
T_x	=	x component of temperature, K
T_0	=	stagnation temperature, K
t_{CN}	=	thickness of contoured nozzle, mm
t_{DA}	=	length of discharge annulus, mm
$\bar{u}$	=	fluid velocity, ms^{-1}
V	=	applied radio-frequency potential, V
V_1	=	fundamental radio-frequency voltage amplitude across a single sheath, V
v_e	=	electron velocity, ms^{-1}
α_v	=	viscosity-temperature exponent
γ	=	ratio of specific heats
Δt	=	time step, s
ϵ_0	=	permittivity of free space, $\text{C}^2\ \text{N}^{-1}\ \text{m}^{-2}$
η_{PC}	=	power-transmission efficiency
λ_{DE}	=	Debye length, m
μ_{ref}	=	reference viscosity at 273.2 K, $\text{N m}^{-2}\ \text{s}$
ν_m	=	electron-neutral collision frequency, MHz

Presented as Paper 5292 at the AIAA Joint Propulsion Conference, Cincinnati, OH, 8–12 July 2007; received 17 August 2007; revision received 9 April 2008; accepted for publication 9 April 2008.

*Ph.D. Candidate; steinw@purdue.edu. Student Member AIAA.
†Assistant Professor; alexeenk@purdue.edu. Member AIAA.
‡Assistant Professor; ihrbud@purdue.edu. Member AIAA.

ρ = fluid density, kg m^{-3}
ω_f = angular applied radio frequency, s^{-1}
ω_p = plasma frequency, s^{-1}

I. Introduction

IN THE last decade, government agencies, military, and industry have recognized the need to deploy small satellites and spacecraft. Six main attributes of small spacecraft dictate design: modularity, maneuverability, maintainability, lifetime, autonomous operation, and launch/hardware cost [1]. As the spacecraft size is reduced, the propulsion wet mass becomes a more significant portion of the overall system mass. Chemical and electric propulsion alike have to address these issues yet still deliver comparable propulsive capability within their mission constraints. In particular, electric propulsion systems also have to take into account power limitations. The integration of electric microthrusters relies on reducing both power and voltage requirements while ensuring reliable long-term performance.

Since the 1990s, electric propulsion (EP) has become a vital part of spacecraft propulsion for a wide spectrum of space missions and applications. These systems can provide significant performance benefits compared with conventional chemical systems [2,3]. Commercial satellite manufacturers have embraced EP due to the significant economic advantages as well. To date, electrothermal, electrostatic and electromagnetic systems propel close to 200 spacecraft in various mission scenarios spanning from low Earth orbit to interplanetary trajectories [4]. However, these systems employ electric thrusters, which function best at power levels greater than 1 kW.

In general, microsatellites can draw power from two sources: solar arrays or batteries. The main power bus of a typical microspacecraft operates well below 100 V and may deliver power levels up to only 100 W. Many state-of-the-art micropropulsion systems use electrostatic acceleration mechanisms to generate thrust: namely, ion [5], Hall [6], field emission electric propulsion (FEEP) [7], and colloid thrusters [8]. Other successful EP-based micropropulsion systems encompass micropulsed plasma thrusters [9], vacuum arc thrusters [10], and microwave electrothermal thrusters [11]. All of these systems require high operating voltages (hundreds to thousands of volts), all of which exceed available voltages on microspacecraft. Power processing units must provide voltage conversions between the main bus and the microthruster, thus adding to the cost and weight of the spacecraft. Extremely high potential differences can also be present, thus increasing the risk of undesirable discharges that can damage sensitive instrumentation or compromise satellite subsystems. Further, these high voltages preclude a direct-drive scheme, which could reduce the amount of power processing to an absolute minimum. A survey of current electric micropropulsion options is given in Table 1 in which representative chemical micropropulsion systems (cold gas, mono-, and bipropellant [13–15]) are also included for comparison.

Electric micropropulsion systems can afford significantly higher specific impulse over chemical propulsion systems, yielding a substantial reduction in the propulsion system wet mass, but it is important that the thruster's power subsystem does not outweigh this benefit. The power supply for an electric thruster is the largest contributor to the propulsion subsystem with regard to mass and volume [16]. On average, thruster power supplies are two to three times more massive than the thruster itself.

Lifetime issues must also be carefully considered. Microthrusters must endure extreme operating conditions and environments, making extended lifetime tests an integral part of technology development [17,18]. Furthermore, erosion of accelerator electrodes commonly used in colloid and FEEP-type propulsion systems are significantly lifetime-limited by the processes they use to generate thrust. Other lifetime issues are backsputtered particles, secondary electron impingement on emitter tips, diminished insulator properties due to propellant condensation between electrodes, and electron impingement from neutralizers, which can cause overheating [19].

An alternative micropropulsion concept is the radio-frequency gas-discharge (RFGD) microthruster. This type of thruster is classified as an electrothermal system and has the potential to overcome these severe microsatellite constraints. A capacitively coupled applied-frequency discharge (RFCCD) between coaxial electrodes provides propellant heating and thermodynamic expansion of the gas generates thrust.

Applied-frequency discharges have been studied extensively for a variety of applications over the past decades and, consequently, there is a vast body of literature available regarding the theory, modeling, and plasma characteristics of such discharges [20,21]. Preliminary proof-of-concept experiments [22] on the application of applied-frequency discharge for propulsion explored electrode wear by comparing dc and applied-frequency operation at comparable levels of power, mass flow rate, and electrode separation. The applied-frequency mode showed favorable results with respect to surface condition and discharge stability. The propulsive capabilities of this concept rely on macroscopic parameters such as geometry (electrode separation), discharge pressure, applied frequency, and applied voltage. These parameters are strong determining factors for plasma formation and the plasma characteristics, which ultimately affect fluid heating, electrode erosion, and thus microthruster performance.

This type of thruster exhibits other beneficial attributes in addition to electrode erosion reduction. Micro- and nanosatellites are limited in mass, size, and available power, but are still required to perform missions similar to those of larger satellites. An RFGD microthruster can meet these requirements by providing the required performance with a system that is comparatively lighter than most traditional electric propulsion systems. This is achieved through the miniaturization of the power-conditioning systems, along with the reduction of thruster size. With power requirements much less than most mainstream electric propulsion systems (10–100 W compared with 1–10 kW), the power-conditioning units for RFGD microthrusters can be made much lighter. Small size/mass and extended operational lifetime make RFGD an attractive candidate to fulfill the niche of low-power, lightweight, cost-effective propulsion.

The main goals of this investigation are to develop an efficient computational approach to model applied-frequency discharges and apply it to simulations of a gas-discharge microthruster for various parameters: namely, electrode geometry, pressure, applied voltage, and applied frequency. This paper summarizes results of computational modeling, which applies particle-in-cell (PIC) and direct simulation Monte Carlo (DSMC) simulations to achieve these goals.

Table 1 A survey of current micropropulsion options

Technology	Electrostatic		Electromagnetic	Electrothermal	Chemical	
	Hall/ion	FEEP/colloid	Micropulsed plasma thrusters and vacuum arc thrusters	Microwave electrothermal thrusters and microresistojet	Cold gas	Liquid
Thrust	1–20 mN	1 μ–1.5 mN	0.03–2 mN	$\leq$ 5 mN	0.5–50 mN	1 μN–200 mN
I_{sp}	1000–3700 s	450–9000 s	200–3000 s	50–250 s	40–80 s	100–315 s
Power	50–300 W	1–100 W	$\leq$ 10 W	5–300 W	——	——
Voltage	100–1000 V	1–10 kV	kV	1–10 V[a]	——	——
Thruster size	$\leq$ 5 cm ϕ	$\leq$ 800 cm^3	——	1–25 cm^3	0.1–10 cm^3	0.1–10 cm^3
Thruster mass	$\leq$ 1 kg	0.1–1 kg	0.06–0.5 kg	0.1–1 kg	0.01–0.5 kg	0.01–0.5 kg

[a]DC voltage for microresistojets [12].

II. Background Theory

A. Principles of Microthruster Operation

Radio-frequency gas discharges can be divided into two main categories: inductively coupled and capacitively coupled discharges. Inductively coupled discharges involve electromagnetic induction and create an electric field with closed field lines. In capacitively coupled discharges, a voltage is applied across electrodes, similar to a capacitor, for which the field lines intersect the electrodes.

An RFCCD is a type of discharge created by oscillating the applied potential across two electrodes at radio frequencies. The structure of an RFCCD, as well as its governing principles, is functionally similar to that of a dc glow discharge, albeit being symmetric in nature. A dc glow discharge is composed of four major regions (the positive column, cathode fall, anode fall, and negative glow/Faraday dark space), is macroscopically time-independent, and primarily uses conduction currents [20].

Conversely, the RFCCD is time-variant, operates using both displacement and conduction currents, and consists of two major regions. The discharge is composed of a central quasi-neutral region, which is analogous to the positive column of a dc glow discharge and sheath regions that exist between the quasi-neutral region and each electrode. The sizes of each region depend on the operating pressure, applied voltage, and relative size of each electrode [23]. A schematic of a typical coaxial RFCCD is given in Fig. 1. The creation of sheaths represents a change in electron/ion number density due to electron/ion diffusion into the electrode itself and for which the structure oscillates with the applied field.

The electron and ion motions within the gas discharge are governed by the applied electric potential and momentum transfer due to collisions with neutral gas molecules [20]. Coulomb collisions between ions and electrons can be neglected for an applied-frequency discharge thruster of this design due to weak ionization (typically, $n_i/n < 10^{-3}$). The oscillations of ions and electrons in a gas discharge are due to a combined effect of two processes: namely, the drift of charges in an electric field and momentum transfer due to collisions. The frequency of such oscillations depends on the effective collision frequency of momentum transfer between charged particles and gas neutrals ν_m and the applied frequency ω_f. The ratio between the two frequencies is a nondimensional number that characterizes the collisional regime. In a limiting case, when $\omega_f/\nu_m \ll 1$, the plasma can be described as a collisional continuum governed by the electrohydrodynamic equations. Conversely, for $\omega_f/\nu_m \gg 1$, the ions and electrons undergo free oscillations in a collisionless manner that can be described by ballistic-type models. In the transitional regime between the continuum and collisionless plasmas, a kinetic description based on the distribution function of charges is required. For argon, the effective frequency of momentum transfer due to plasma collisions is estimated as [24]

$$\nu_m = \nu_{m0} P\left(\frac{T_{\text{ref}}}{T}\right) \tag{1}$$

with pressure in torr and $\nu_{m0} = 5.3 \times 10^9$ Hz/torr for argon. Figure 2 shows the collisional regimes of argon discharge as a function of gas pressure and applied frequency. For pressures larger than 10 torr, the plasma lends itself to a continuum description for frequencies up to 1 GHz. On the other hand, for pressures below 10 torr, the discharge is in a noncontinuum regime for the whole applied-frequency range. Therefore, to accurately predict argon discharge characteristics at low and moderate pressures, this study applies a kinetic approach based on the particle-in-cell method with Monte Carlo collisions (PIC/MCC).

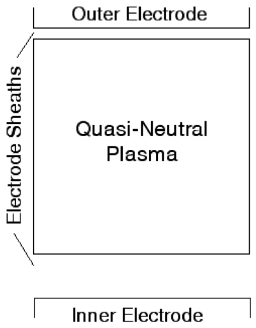

Fig. 1 Schematic of a typical coaxial RFCCD.

In an RFCCD, the applied-frequency potentials and currents are applied directly to the electrodes, creating high-voltage capacitive sheaths between the electrodes and the bulk plasma. These sheaths lead to a stochastic/collisionless heating of the plasma at the plasma boundaries and can become a large component of the total plasma heating at lower pressures. At higher pressures and applied frequencies, the sheaths recede in width and collisional power transmission dominates [20]. Thus, two major types of fluid heating are present in an RFCCD under the conditions considered in this investigation.

The primary method of fluid heating is ohmic heating. Ohmic heating is predominately caused by collisional momentum transfer between the plasma and neutral molecules and can be expressed per unit area as [20]

$$\bar{S}_{\text{ohm}} = \frac{1}{2}\frac{m_e \nu_m d_{\text{gap}}}{e^2 n_o} J_1^2 \tag{2}$$

Stochastic heating is the second major heating mechanism present in an RFCCD. Stochastic heating arises from a velocity change due to the time-varying fields present along the sheath boundaries. When the mean free path of an electron exceeds the width of the sheath, the electron is reflected by the space charge potential present at the sheath boundary. This is akin to throwing a tennis ball at a large wall, except in this case, the wall oscillates at the applied frequency. Thus, energy is imparted to the electrons by the moving sheath boundary and the fluid is effectively heated. A relation for the stochastic heating per unit area in a single sheath is given as [20]

$$\bar{S}_{\text{stoch}} = \frac{1}{2}\frac{m_e \bar{v}_e}{e^2 n_o} J_1^2 \tag{3}$$

Substituting the fundamental current density

$$J_1^2 \propto n_s e \epsilon_0 \omega_f^2 T_e^{1/2} V_1^{1/2} \tag{4}$$

into Eqs. (2) and (3), one can obtain the relations for ohmic and stochastic heating in a more useful form:

$$\bar{S}_{\text{ohm}} \propto \frac{m_e n_s}{e n_o} \nu_m d_{\text{gap}} \epsilon_0 \omega_f^2 T_e^{1/2} V_1^{1/2} \tag{5}$$

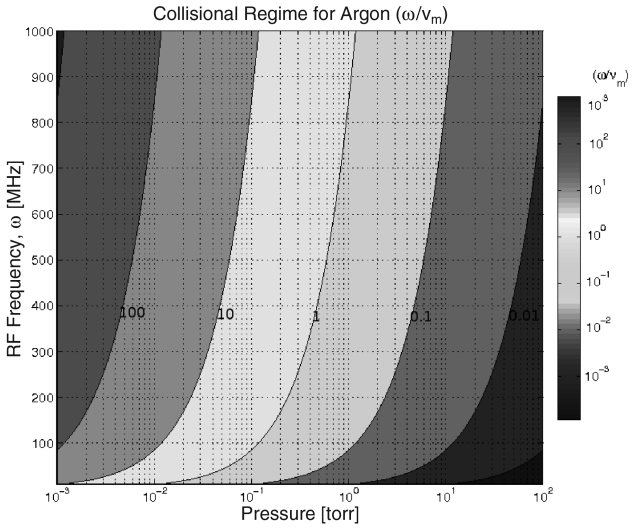

Fig. 2 Collisional regimes for argon as a function of applied frequency and pressure at 300 K.

$$\bar{S}_{\text{stoch}} \propto \left(\frac{m_e}{e}\right)^{1/2} \epsilon_0 \omega_f^2 T_e^{1/2} V_1 \tag{6}$$

Ohmic heating can also become a large heating component within high-voltage collisional sheaths. This component can be expressed for each sheath using [20]

$$\bar{S}_{\text{ohm,sh}} \propto \frac{m_e \epsilon_0}{2e^2 n_s} \nu_m d_{\text{gap}} \omega_f T_e^{-1/2} V_1^{3/2} \tag{7}$$

Combining Eqs. (1) and (5–7), the total absorbed power within the discharge can be written as

$$\mathbb{P}_{\text{abs}} \propto \left\{ \left[\frac{n_s}{n_o} \frac{P d_{\text{gap}}}{T_{ng}} V_1^{1/2} + V_1 \right] \omega_f^2 T_e^{1/2} + \frac{\omega_f P V_1^{3/2}}{n_s T_{ng} T_e^{1/2}} \right\} A_{\text{surf}} \tag{8}$$

Assuming that stochastic heating is small compared with ohmic heating over the range of conditions in this investigation and the ratio of electrode radii is fixed to yield a 50-Ω impedance in vacuo, Eq. (8) can be written in terms of the input parameters (pressure, temperature, inner radius, applied voltage, and applied frequency) as

$$\mathbb{P}_{\text{abs}} \propto \left\{ \frac{n_s}{n_o} \omega_f^2 V_1^{1/2} T_e^{1/2} r_0 + \frac{\omega_f V_1^{3/2}}{n_s T_e^{1/2}} \right\} \frac{P r_0 L_{\text{ch}}}{T_{ng}} \tag{9}$$

Equation (9) shows that the power absorbed by the fluid is directly proportional to the discharge pressure, inner radius, applied potential, and the applied frequency, but is inversely proportional to neutral temperature. The only unknown quantities in Eq. (9) are a discharge shape factor n_s/n_o, the number density at the beginning of the sheath n_s and the electron temperature T_e. These quantities have more complex relations with the input parameters, but can be determined once the discharge is known.

B. Previous and Related Work

Although this thruster technology is relatively new, applied-frequency technology has been previously used as a propulsion mechanism, albeit in different ways [25–31]. Although past research has not been extensively performed using an RFCCD for propulsive applications, it has been used extensively for several decades in the field of etching and sputtering [20,21]. Etching/sputtering research is primarily devoted to a low-pressure discharge in argon to effectively sputter or etch a target material, but is not used for heating a fluid. Although the process is effectively the same, the objectives of a sputtering/etching discharge are the opposite of those required for thruster operation. Work has also been done regarding the use of different gases within the discharge [32–37], which illustrates possible benefits of using various propellants.

The most technically similar work was performed in 1999 [22,38]. This experimental work focused primarily on investigating electrode erosion and the effect of characteristic operating parameters such as mass flow, applied frequency, applied power, and electrode separation distance. It was performed with a large proof-of-concept thruster having an inner electrode diameter of approximately 5 cm. This work demonstrated a reduction in electrode erosion when compared with operation in a dc mode, as well as an appreciable rise in temperature within the thruster.

III. Modeling Approach

The presented modeling approach combines both PIC and DSMC methods to evaluate the performance of RFGD microthrusters. The control parameters used in this investigation include pressure, electrode size, applied frequency, and applied voltage. These control parameters range from 100 to 1000 MHz for the applied frequency, voltages between 10 and 500 V, and pressures varying between 0.1 to 10 torr. The geometry of the thruster corresponds to prototypes studied experimentally at Purdue University. Figure 3 shows a schematic of the thruster. The discharge annulus is formed by coaxial electrodes, for which the radii obey the impedance law for coaxial transmission lines in vacuum. The length of the discharge annulus is

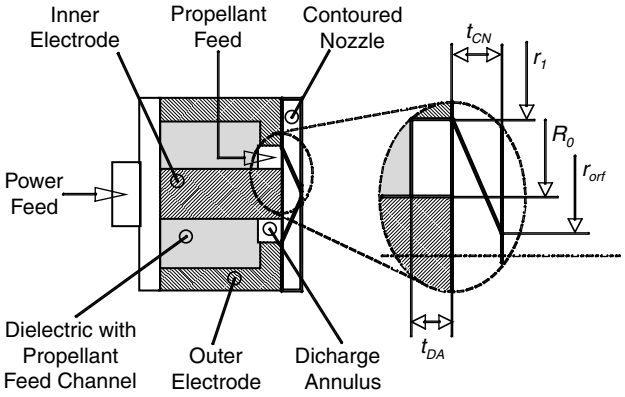

Fig. 3 Thruster schematic.

$t_{\text{DA}} = 5$ mm. The radius of the inner electrode is varied between 1 and 5 mm, and the radius of the outer electrode adjusts according to the impedance law, maintaining 50 Ω in vacuum. Downstream of the discharge annulus is a contoured nozzle plate. This plate is $t_{\text{CN}} = 6.5$ mm thick and features an orifice of radius $R_{\text{orf}} = 1$ mm.

A. Particle-In-Cell/Monte Carlo Collision Modeling

The PIC/MCC method is currently the most powerful approach for kinetic plasma modeling in the subcontinuum regime [39–41]. PIC/MCC simulations are used in this model to determine plasma characteristics within the coaxial discharge chamber. The charged test particles in the PIC/MCC method move in the applied electric field, and representative collisions between charged and neutral particles are calculated using the Monte Carlo method. Our model uses XPDC1, a one-dimensional, bounded, cylindrical plasma simulation code developed by the Plasma Theory and Simulation Group at the University of California at Berkeley. The argon collisional model employed in XPDC1 includes electron-neutral ionization, lumped excitation, and elastic scattering collisions using Lawler–Kortsghagen cross sections [42]. Ion-neutral charge exchange and elastic scattering collisions are also incorporated.[§] The computational parameters of the PIC model were chosen to meet the following criteria for numerical accuracy:

1) The number of cells $nc \geq 2d_{\text{gap}}/\lambda_{\text{DE}}$.

2) The time step $\Delta t \leq 0.2/\omega_p$ and $\Delta t \leq 1/\omega_f$.

3) The ratio of computational to physical particles is determined such that $nc2p$ results in ≈50–100 computational particles per cell at steady state.

The discharge is simulated until the plasma number densities stabilize within ±1% of the average number density taken over the last 1000 applied-frequency cycles.

1. *Constant-Temperature Model*

The first temperature model employed in this investigation is a constant-temperature model. In this model, the neutral gas temperature within the PIC simulation remains constant throughout the discharge and is not affected by the plasma. The neutral-gas-temperature distribution is later calculated separately, after the PIC simulation reaches a steady state, for use as an input condition in the DSMC simulation. The neutral gas temperature is calculated based on the period-averaged electric field and the ion current density by solving 1-D heat conduction within the coaxial electrode gap [43]:

$$-\frac{1}{r}\frac{\partial}{\partial r}\left[rk\frac{\partial T}{\partial r}\right] = \langle j \cdot \bar{E} \rangle \tag{10}$$

This model is subject to the boundary conditions of a fixed temperature of 300 K at both the inner and outer electrodes, where T is the gas temperature, k is the thermal conductivity, j is the ion

[§]Data available online at http://ptsg.eecs.berkeley.edu/ [retrieved 12 December 2006].

current density, and E is the electric field. The angle brackets on the right-hand side denote period-averaged quantities.

2. Gas Heat Transfer Model

The original code XPDC1 was augmented to incorporate real-time changes in the discharge as a result of plasma heating. Because the main goal of these simulations is to study the performance and behavior of a microthruster that uses an RFCCD to heat a working fluid, neutral gas heating effects need to be taken into consideration. XPDC1 was originally written to model different plasma discharges at lower pressures where modeling via PIC simulations is efficient. Within this realm, heat transfer to the neutral gas species can be considered negligible and thus is not simulated. This investigation borders on the periphery of this model and must range from a collisionless regime to that of a continuum, in which changes in neutral gas temperature become more prevalent. Thus, gas-temperature variation must be incorporated to make the simulation self-consistent within subcontinuum and continuum regimes.

The neutral gas temperature is calculated based on period-averaged power transmission into the fluid by solving 1-D heat conduction in the coaxial electrode gap with fixed-temperature boundary conditions. This is traditionally solved using Joule heating in diffusion-drift approximation [43]. In PIC simulations, it is possible to use the actual power transmission that occurs with the various types of plasma-neutral collisions:

$$-\frac{1}{r}\frac{\partial}{\partial r}\left[rk\frac{\partial T}{\partial r}\right] = \langle \mathbb{P}_f \rangle \tag{11}$$

where T is the gas temperature, k is the thermal conductivity, and the angle brackets on the right-hand side denote a period-averaged quantity. Four power-loss mechanisms exist in this regime, namely, due to elastic $\mathbb{P}_C^{\mathrm{el}}$, charge exchange $\mathbb{P}_C^{\mathrm{cx}}$, ionization $\mathbb{P}_C^{\mathrm{iz}}$, and excitation collisions $\mathbb{P}_C^{\mathrm{ex}}$. The power transmitted into the fluid consists of only the first two power-loss mechanisms and can be written as

$$\mathbb{P}_f = \mathbb{P}_C^{\mathrm{cx}} + \mathbb{P}_C^{\mathrm{el}} \tag{12}$$

Electrons can collide with neutrals via elastic, ionization, or excitation collisions, whereas ions and neutrals collide elastically or via charge exchange.

Elastic and charge-exchange collisions directly transfer energy from the plasma to the neutrals. Conversely, ionization and excitation collisions serve a different purpose. Ionization collisions create ion-electron pairs that help sustain the plasma and offset diffusion losses. The remaining energy not used to ionize the neutral atom is transferred directly to the energy of the new ion/electron pair. The power lost to excitation collisions is regarded as a similar loss mechanism. It is not used to heat the working fluid, but is lost via the excitation of electrons within the outer valence shells of the neutral molecules, which is then reemitted via the glow. Although it is understood that some of the photonic power reemitted from the excited neutrals could be used to heat the fluid, it is believed to be negligible in comparison with the sum of the other heating mechanisms and is not modeled in this simulation.

The neutral gas temperature is calculated using Gaussian elimination with partial pivoting every 1000 time steps. A distribution of the time-averaged power transmitted into the fluid is used to solve for the temperature distribution throughout the discharge. The thermal conductivity of argon is calculated using a power-law temperature model and the temperature distribution at the previous time step:

$$k = \frac{3}{2}C_p\mu_{\mathrm{ref}}\left(\frac{T}{T_{\mathrm{ref}}}\right)^{\omega} \tag{13}$$

with

$$\mu_{\mathrm{ref}} = 2.117 \times 10^{-5}\ \mathrm{Nm^{-2}\,s} \qquad C_p = 524\ \mathrm{J\,kg^{-1}\,K}$$
$$T_{\mathrm{ref}} = 273.2\ \mathrm{K} \qquad \omega = 0.81$$

The temperature boundary conditions for this investigation were set to 300 K, which is typical for the initial stage of thruster operation. The wall thermal boundary conditions are dependent more on the specific thruster design and operating conditions and were set to 300 K for this investigation.

B. Direct Simulation Monte Carlo Modeling

The DSMC method is applied to model the neutral gas expansion in the microthruster nozzle. A kinetic approach to modeling neutral gas flow in the thruster is needed due to significant effects of rarefaction in the operating pressure range (mtorr–torr). The value of the Knudsen number based on the orifice diameter of 2 mm is about 0.04 at $P = 1$ torr and $T = 300$ K. The axisymmetric DSMC code SMILE (statistical modeling in a low-density environment) [44] is applied with a variable-hard-sphere model, a molecular diameter of 4.17×10^{-10} m, and a viscosity-temperature exponent $\alpha_v = 0.31$ for argon.

The applied-frequency thruster performance parameters such as thrust, mass flow rate, and specific impulse are calculated based on the DSMC solution at the orifice exit plane and compared with those for cold-gas expansion for the same geometry and similar operating conditions. For nonequilibrium flow, thrust is defined as [45]

$$F = \int_A \rho\left\{\int_a^b \int_{-\infty}^{\infty}\int_0^{\infty} u^2 f\,\mathrm{d}u\,\mathrm{d}v\,\mathrm{d}w\right\}\mathrm{d}A \tag{14}$$

where u, v, and w represent the velocity components. The thrust can then be calculated in terms of sampled parameters in the DSMC simulation using

$$F = \int_A \left(\rho\bar{u}^2 + P\frac{T_x}{T}\right)\mathrm{d}A \tag{15}$$

where T_x represents the axial temperature component. Also, the ideal microthruster performance can be calculated assuming isentropic expansion through a smooth sonic nozzle into vacuum as follows:

$$\dot{m} = \left(1 + \frac{\gamma - 1}{2}\right)^{\frac{\gamma+1}{2(1-\gamma)}}\sqrt{\frac{\gamma}{RT_0}}P_0A^* \tag{16}$$

$$gI_{\mathrm{sp}} = \sqrt{\frac{2RT_0(\gamma+1)}{\gamma}} \tag{17}$$

$$F = I_{\mathrm{sp}}\dot{m}g \tag{18}$$

Approximately 5 million computational particles and about 1 million collision cells with a time step of 30 ns were used in the DSMC simulation that took about 24 h on eight processors of a SunFire 4600.

IV. Results and Discussion

The primary goal of this investigation is to discover overall RFGD microthruster performance trends by comparing how the four design variables (chamber pressure, inner radius, applied frequency, and applied voltage) affect thrust, specific impulse, power transmission, and power-transmission efficiency. For this investigation, the ratio of the inner and outer electrodes is fixed such that the thruster impedance (in vacuo) is approximately 50 Ω.

Performance analysis is performed in three major sections. It begins with an initial study over a range of design variables and investigates their effect on the characteristics of the gas discharge. This analysis provides general trends for the dependence of the various types of power loss and power-transmission efficiency over a range of input conditions. This section primarily focuses on the effects of applied frequency, discharge pressure, inner radius, and applied voltage. In the second section, additional analysis is performed regarding the effect of heat transfer and the neutral gas

temperature. From these results, a microthruster design case is chosen and used for further DSMC analysis in the last section to determine overall thruster performance. In the last two sections, both the constant-temperature model and the gas heat transfer model are employed to illustrate the importance of gas heat transfer within the discharge and how plasma heating can affect thruster performance. There are two general types of power losses considered in this investigation: that lost to collisions and that lost to electrode impact. Collisional power loss is further divided into four types (power lost to elastic, charge exchange, ionization, and excitation collisions), each influencing performance in a different way. Ionization and particle diffusion dominate the net particle-generation rates, whereas recombination and convective losses have been found to be negligible in discharges operating under these conditions [46].

The RFGD microthruster performance is characterized chiefly by its ability to efficiently convert energy of the applied electric field into the propellant enthalpy and then to kinetic energy in the nozzle expansion. This ability can be characterized through a ratio of power transmission into the fluid over the total absorbed power:

$$\eta_{\mathrm{PC}} = \frac{\mathbb{P}_f}{\mathbb{P}_f + \mathbb{P}_C^{\mathrm{cx}} + \mathbb{P}_C^{\mathrm{in}} + \mathbb{P}_w} \tag{19}$$

This parameter η_{PC} is an indicator of how well a given thruster design can heat the working fluid for a given amount of total power delivered to the thruster. This can also provide a metric for evaluating electrode erosion. Although particle collisions with the electrodes cannot be totally eliminated in general, conditions can be sought that effectively minimize the power loss to the electrodes.

This analysis also considers limitations in applied power. The PIC/MCC code incorporates either a voltage-limited or current-limited source, but does not include any type of power limitation. This poses a problem because the applied power will be physically limited by the type of power supply that is ultimately used. For the scope of this analysis, cases that have a total power absorption of approximately 50–75 W are considered desirable for a thruster of this type and mission. Other cases that provide a power consumption outside this range are presented to express overall trends, but are not used for thruster design.

A. Gas-Discharge Analysis

The first step to understanding RFGD microthruster performance is to investigate the influence of the various input parameters (namely, discharge pressure, applied potential, applied frequency, and electrode geometry) on the discharge characteristics. The first section investigates the effects of pressure and frequency on both the power transmitted into the fluid and the power-transmission efficiency for two different inner radii and two applied voltages. The second section achieves a similar aim by investigating microthruster performance by varying both the inner radius and applied voltage at a fixed pressure and frequency.

1. *Effects of Pressure and Frequency*

This section explores how discharge pressure and applied frequency affects microthruster performance for different inner radii and applied voltages. Figures 4 and 5 illustrate the effects of pressure and applied frequency on both the power transmitted into the fluid and the power-transmission efficiency. Coulomb-collision and diffusion-limited regions are also identified in Figs. 4 and 5. In the coulomb-collision region, the assumption $n_i/n < 10^{-3}$ is violated and thus provides poorly modeled results. This occurs in regions of low pressure and high plasma number density. Also, within the diffusion-limited region, the electron diffusion to the electrodes is too large compared with electron–ion production and the plasma discharge becomes unsustained. This occurs again at lower pressures and lower voltages where ionization is poor and diffusion to the electrodes is high.

These results show that the power transmitted into the fluid is directly proportional to both the applied frequency and the discharge pressure. An increase in pressure increases the plasma-neutral collision frequency [Eq. (1)] and thus allows more power to be

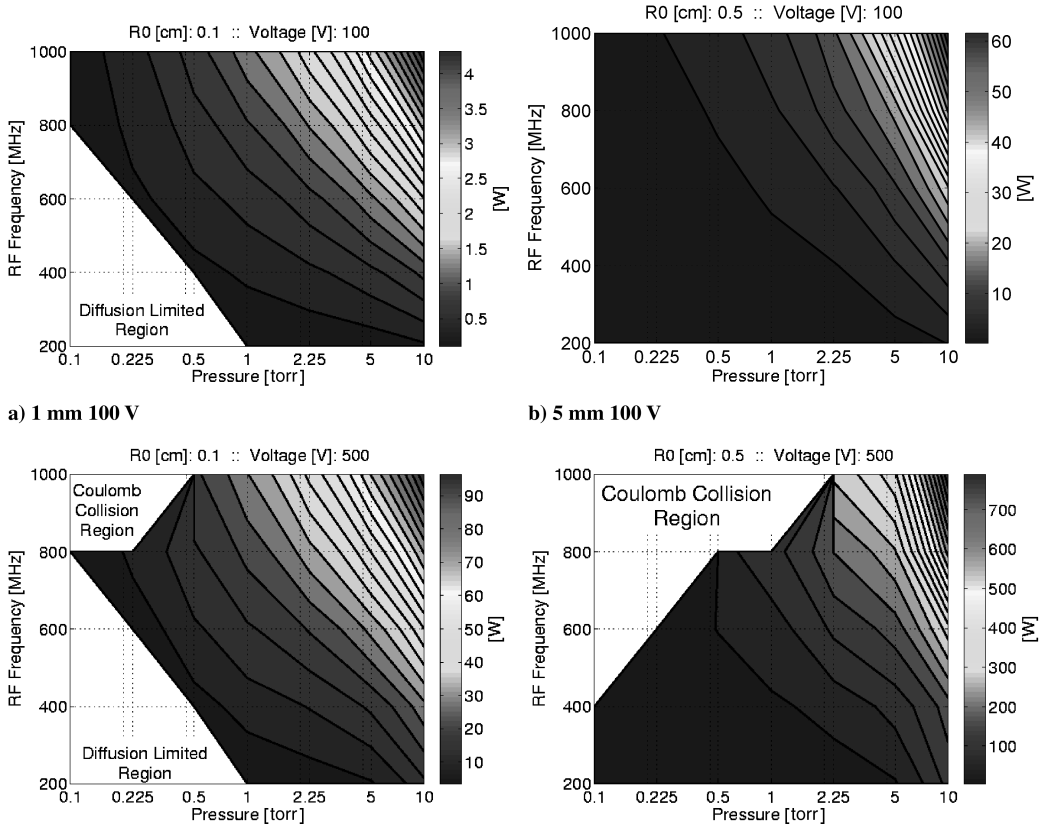

a) 1 mm 100 V **b) 5 mm 100 V**

c) 1 mm 500 V **d) 5 mm 500 V**

Fig. 4 Power transmitted into the fluid (in watts).

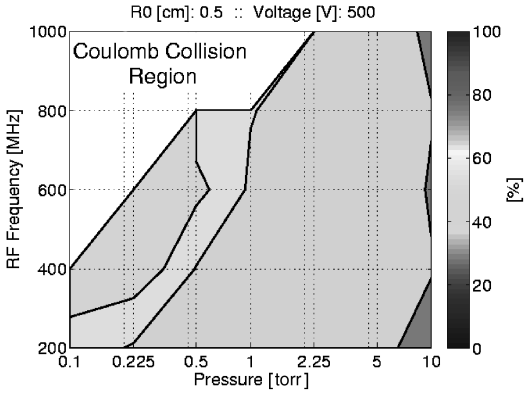

Fig. 5 Power-transmission efficiency η_{PC} for the 5-mm, 500-V case.

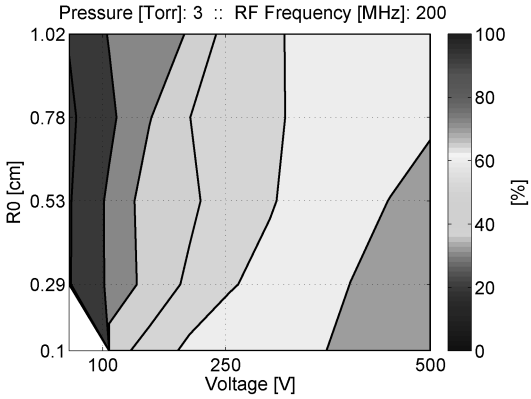

Fig. 7 Power-transmission efficiency η_{PC}.

transmitted into the fluid. Increasing the applied frequency increases the sheath current density, thus increasing the amount of power transmitted into the fluid via ohmic heating [Eq. (4)]. Both the relationship for applied frequency and pressure are also reflected in Eq. (9). Figure 5 shows that the power-transmission efficiency improves as the plasma becomes more collisional and scales with an increase in pressure or a decrease in frequency, as in Fig. 2.

Figure 4 also shows that with a general increase in either the inner radius or the applied potential, the power transmitted into the fluid increases. Figure 5 shows that increasing the voltage increases the power-transmission efficiency, but conversely, an increase in inner radius decreases the power-transmission efficiency. These effects are further discussed in more detail in Sec. IV.A.2.

2. *Effects of Inner Radius and Voltage*

The second section of this analysis observes the effects on microthruster performance regarding changes in inner radius and applied potential. Changes in these two parameters dictate variations in the reduced electric field and hence the structure of the discharge itself. For this investigation, the outer electrode radius, and thus the thruster geometry, is defined such that the thruster impedance (in vacuo) is approximately 50 Ω. Thus, varying the inner electrode alone scales the interelectrode gap and consequently the discharge volume.

Investigating the variation of the inner radius and applied potential produces information regarding thruster scalability and the applicability of using satellite bus voltages directly, without any need for voltage conditioning. It is believed that there are effective limits on both the inner radius (i.e. interelectrode gap distance) and the applied potential corresponding to limits in the discharge physics. The applied potential and inner radius must be in a configuration for which a discharge cannot only be initiated, but also sustained. Thus, a balance between the ionization and plasma diffusion must be achieved to create and sustain the discharge. If the ionization rate is too low or the diffusion rates are too high, a discharge cannot be sustained. Also, the physical characteristics of the discharge will change, shifting the discharge from an α type to that of a γ type or even possibly that of a glow-arc transition.

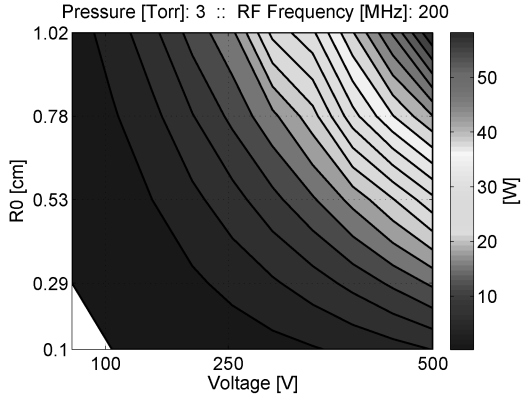

Fig. 6 Power transmitted into the fluid (in watts).

The limits of these two parameters range from 0.5 mm to 1 cm for the inner radius and 10 to 500 V for the applied potential. The ranges of these variables were determined from both previous studies [47] and the desire to investigate the lower operating limits for both the applied potential and thruster size. The power transmitted into the fluid and the power-transmission efficiency for this study are shown in Figs. 6 and 7.

As aforementioned, one can see the power transmitted into the fluid increase with an increase in both potential and inner radius. Because the power transmitted into the fluid is mainly composed of the power lost to charge-exchange collisions, any trends shown in $\mathbb{P}_f$ can be explained via trends derived from $\mathbb{P}_C^{\text{cx}}$. Increasing the applied potential increases the potential drop through each sheath, thus causing the ions to accelerate faster within each sheath, thus increasing the power transmission for each ion-neutral collision. An increase in inner radius increases the volume of the discharge that translates into an increased number of collisions within the discharge at a constant number density, which correspondingly increases the total amount of power transmitted into the fluid. These relations can be shown in Eq. (9).

In terms of the power-transmission efficiency, higher voltages and lower inner radii are preferred. This is mainly related to how the power lost to charge exchange and power lost to excitation collisions change. As the voltage is increased, the voltage drops across the sheaths become more pronounced, leading to an increase in charge-exchange power loss. However, increasing the voltage has a lesser effect in the quasi-neutral region, which remains near a constant potential. Power lost to charge exchange (the primary component of $\mathbb{P}_f$) increases at a faster rate than that of the power lost to excitation collisions (the primary inefficiency) and thus increases the power-transmission efficiency with an increase in voltage. An increase in inner radius has little effect on the quasi-neutral and sheath regions within the discharge. Therefore, there is a less pronounced effect with a change in inner radius, which is shown in Fig. 7.

This study also found lower limits to both the inner radius and potential. Discharges simulated at 10 V exhibited very little ionization and not enough to sustain the discharge. Also, discharges simulated with an inner radius of 0.5 mm could not be sustained regardless of potential. Mainly, the electron diffusion rates were too high to fully sustain the discharge.

Table 2 Comparison of estimated statistical errors for the different power-loss mechanisms

Conditions		% $\mathbb{P}_C^{\text{in}}$	% $\mathbb{P}_C^{\text{cx}}$	% $\mathbb{P}_C^{\text{ex}}$	% $\mathbb{P}_f$	% $\mathbb{P}_W$
1 mm	100 V	10	6	5	5	23
5 mm	100 V	18	10	7	9	47
1 mm	500 V	18	10	9	10	48
5 mm	500 V	25	14	10	14	79
3 torr	200 MHz	28	6	6	6	60

Table 3 Comparison of data with different temperature models

Constant-gas temperature model							
Conditions:				$\bar{T}_{\text{gas}}$, K	$\bar{n}_e$, m^{-3}	$\mathbb{P}_f$, W	η_{PC}
3 torr	200 MHz	3 mm	59 V	300.0	1.57e17	0.30	0.25
3 torr	200 MHz	5 mm	500 V	300.0	1.76e18	32.5	0.69
10 torr	1000 MHz	1 mm	100 V	300.0	7.72e18	4.57	0.30
1 torr	600 MHz	1 mm	500 V	300.0	5.30e18	16.8	0.64
Gas Heat Transfer Model							
Conditions:				$\bar{T}_{\text{gas}}$, K	$\bar{n}_e$, m^{-3}	$\mathbb{P}_f$, W	η_{PC}
3 torr	200 MHz	3 mm	59 V	312.4	1.35e17	0.44	0.18
3 torr	200 MHz	5 mm	500 V	605.9	1.12e18	30.2	0.68
10 torr	1000 MHz	1 mm	100 V	430.4	5.90e18	6.26	0.33
1 torr	600 MHz	1 mm	500 V	558.2	3.04e18	14.8	0.49

3. Estimated Statistical Errors of PIC/MCC Calculations

The estimated statistical errors for the various power-loss mechanisms are shown in Table 2 and are calculated by taking the ratio of the standard deviation of the data to its average. The values presented in Table 2 represent an average of the statistical errors for all the cases simulated at the specified conditions. The average statistical error in both the electron and ion number densities for all conditions is less than 1%.

The power lost to the walls presents the largest statistical error for these cases, with the power lost to ionization collisions being the next largest. These errors can introduce large uncertainties in the calculation of the power-transmission efficiency, especially at lower values. For regions in which the power-transmission efficiency is relatively high for instance, the 5-mm inner radius 500-V cases, the magnitude of the power lost to ionization and the walls is relatively small when compared with that of the power transmitted into the fluid or the power lost to excitation. This is mainly because the power transmitted into the fluid and the power lost to excitation collisions represent the majority of the power absorption in the discharge. In general, the power lost to the walls and to ionization collisions is relatively smaller than the aforementioned. Thus, as power transmission into the fluid increases, the overall effect of these statistical errors on the power-transmission efficiency is reduced.

B. Effects of Gas Heat Transfer

To better understand how gas heat transfer affects the characteristics of the plasma discharge and their performance implications on an RFGD microthruster, four cases were analyzed with both temperature models. Each case corresponds to a different power level at a different set of input conditions, and the results from this analysis are shown in Table 3.

The magnitude of the effect that neutral gas heat transfer has on the discharge characteristics depends on the operating conditions of thruster. Over this range of input conditions, the power transmitted into the fluid varies greatly and changes the effect of neutral gas heat transfer in the discharge. Even at a lower power, heat transfer to the neutrals is nonnegligible. As power is transmitted to the neutral gas, the neutral temperature rises, reducing the gas density and thus the neutral collision frequency. This reduces the plasma's effectiveness to transmit power into the fluid and thus reduces the gas temperature, until the discharge becomes stable. Thermal conductivity effects are also nonnegligible, especially for higher-power/higher-temperature discharges. The temperature distributions for these cases are compared in Fig. 8.

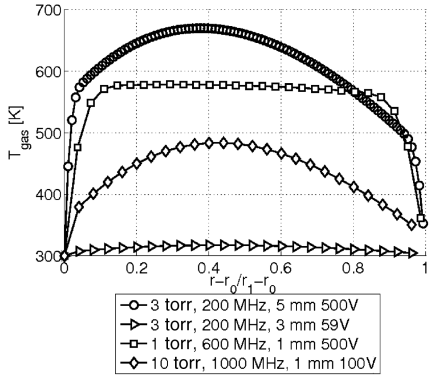

Fig. 8 Comparison of temperature profiles and the gas heat transfer model.

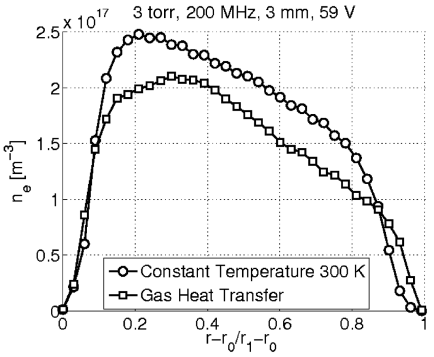

Fig. 9 Comparison of electron number density profiles.

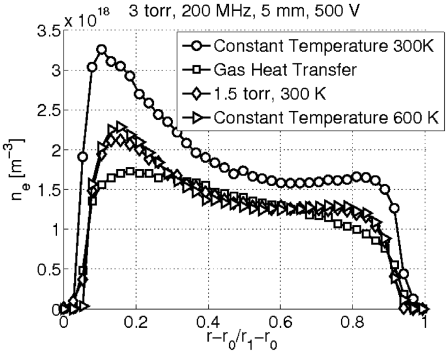

Fig. 10 Comparison of electron number density profiles.

Gas heat transfer not only affects the bulk parameters of the discharge but also affects the shape of the discharge as well. Electron number densities are compared for two cases in Figs. 9 and 10. The presence of higher neutral temperatures in the discharge reduces the electron number densities of the plasma, as aforementioned, but also affects their distribution shape. An increase in neutral temperature effectively reduces the discharge pressure via a reduction in neutral number density. This effect can be shown using the plasma-neutral collision frequency estimated in Eq. (1).

Therefore, similar discharge characteristics should appear if the pressure is raised with an increase in temperature that keeps the plasma-neutral collisional frequency constant. This will not exactly be a one-to-one relation, given that collision cross sections, power transmitted into the fluid, and thermal conductivity are all functions of temperature. Also, there will be effects derived from the shape of the temperature distribution itself, because it is not constant across the discharge. Electron number density profiles and bulk parameters of the 5-mm/500-V case with gas heat transfer are compared with those of a discharge at similar conditions, but with a discharge

Table 4 Comparison of reduced effective pressure on discharge parameters

Model	$\bar{T}_{\text{gas}}$, K	$\bar{n}_e$, m^{-3}	$\mathbb{P}_f$, W	η_{PC}
3 torr, 200 MHz, 5 mm, 500 V				
Constant gas temperature	300.0	1.76e18	32.5	0.69
Gas heat transfer	605.9	1.12e18	30.2	0.68
Constant gas temperature	600.0	1.19e18	13.0	0.66
1.5 torr, 200 MHz, 5 mm, 500 V				
Constant gas temperature	300.0	1.18e18	12.4	0.65

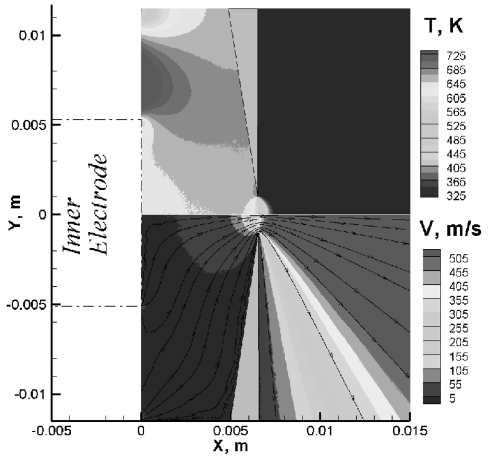

Fig. 11 DSMC calculated temperature contours (top) and *X*-velocity contours and streamlines (bottom) with gas heat transfer.

pressure of 1.5 torr. This reduction in pressure corresponds to the effective increase in average temperature shown by the addition of gas heat transfer and is shown in Fig. 10 and Table 4.

Figure 10 shows the difference in discharge structure with and without gas heat transfer. This is the average neutral gas temperature used in the PIC simulation, not an average of the neutral gas temperature calculated using 1-D heat conduction calculated separately. The presence of neutral gas heat transfer not only reduces the electron number density as expected, but it also reduces the sizes of both presheath peaks.

Two discharges at 1.5 torr/300 K and 3 torr/600 K with constant-temperature profiles were also compared. These two cases show similar discharge characteristics, with the exception of slightly enhanced presheath peaks in the 3-torr case. This illustrates the fact that plasma-neutral collision frequency influences the overall number density of the plasma, but the discrepancies indicate that other factors can influence the discharge shape to a lesser extent.

One can also observe the effects of the neutral temperature distribution by comparing the 3-torr/600-K case with and without neutral gas heat transfer. The similarity of the distributions exhibited in these cases reinforces the hypothesis that the plasma-neutral collision frequency is a primary mechanism for creating similar discharges. Secondary mechanisms, such as the shape of the neutral temperature distribution and thermal conductivity, also play a role in the discharge characteristics. Operating at a higher pressure and a lower temperature is beneficial for better power transmission into the fluid, but does not necessarily mean better power generation by the discharge in general.

C. Microthruster Performance

DSMC modeling was applied to obtain flowfields and thruster performance of the RFGD microthruster at design conditions of 3 torr, 500 V, 5 mm, and 200 MHz. The DSMC computational domain is shown in Fig. 11 and extends from the exit of the discharge chamber/inner electrode wall on the left ($x = 0$) to the converging nozzle (shown in gray) through which the flow expands into a vacuum. The inflow boundary at $x = 0$ corresponds to a constant pressure of 3 torr, zero velocity, and gas-temperature distributions obtained via PIC/MCC simulations using both preceding temperature models (Secs. III.A.1 and III.A.2). The main mechanism for performance gain is through a plasma heating of the propellant by the discharge, but microthruster performance is also affected by heat transfer to the nozzle walls. The effect of heat loss was investigated by considering two different thermal conditions at the nozzle wall boundaries and using temperature distribution derived from the PIC results using the constant-temperature model. The adiabatic nozzle wall is modeled using a zero-energy accommodation coefficient in the Maxwell gas–surface interaction model. Another case was considered with a cooled nozzle wall and the nozzle wall was set to a constant temperature of 300 K. The results of these analyses are given in Table 5.

It can be seen that using an RFCCD can provide notable improvement over using a cold-gas expansion. Heat transfer within the discharge, as well as between the discharge and the thruster walls, can also have a significant impact on the microthruster performance. There are several ways to further increase the specific impulse of an RFGD microthruster. First, a propellant that is easy to ionize (e.g., xenon) and that has a lower molecular weight (e.g., helium) would allow an increase in the specific impulse by a factor of at least two. Second, the discharge at higher pressures would decrease viscous losses and would allow achieving a supersonic flow in the nozzle expansion. For the current thruster configuration and discharge pressure of 3 torr, the Reynolds number at the orifice plane is about 40. At such a low Reynolds number, viscous losses are extremely large and the efficiency of converging–diverging nozzle is even lower than that of an orifice expansion [48]. The experimental and numerical results [48] for gas expansion through nozzles and orifices at low Reynolds numbers indicate that to achieve a supersonic flow, the pressure has to be increased by a factor of about 6. RFCCD at such high pressures can be achieved for millimeter-scale coaxial gaps, if the discharge chamber length increases. If these two mechanisms for increasing the specific impulse of an RFGD microthruster are applied, the specific impulse of such an electrothermal micropropulsion system can approach that of macroscale chemical thrusters.

V. Conclusions

An RFGD thruster was modeled using a combination of PIC and DSMC simulations. It was demonstrated that there is a required minimum applied potential and minimum inner radius for which a discharge can be sustained. Power transmission into the fluid increases with an increase in applied potential, inner radius, applied frequency, or discharge pressure. Power-transmission efficiency increases with an increase in applied potential, an increase in discharge pressure, or a reduction in applied frequency or inner radius. Both of these trends can be explained by changes in the relative magnitudes of charge exchange and excitation power losses or the discharge volume. A gas heat transfer model was successfully implemented within PIC/MCC simulations and illustrates that heat transfer to the neutral gas molecules plays an integral part in

Table 5 Applied-frequency thruster performance using the constant 300 K (CT3K) and gas heat transfer (GHT) temperature models at 3 torr, 5 mm, 500 V, and 200 MHz)

Case	T_{de}, K	F, mN	$\dot{m}$, mg/s	I_{sp}, s	I_{sp} improvement over cold gas
		DSMC results with applied-frequency discharge model			
300-K wall, CT3K	1990	1.29	2.25	58.2	31%
Adiabatic wall, CT3K	1990	1.12	1.27	89.5	102%
300-K wall, GHT	600	1.00	1.73	58.6	32%
Adiabatic wall, GHT	600	1.25	2.00	63.8	44%
Cold-gas expansion	300	1.33	3.05	44.3	
		Ideal nozzle results			
300-K expansion	300	1.9	3.7	51.3	
600-K expansion	600	1.8	2.5	72.5	

developing the plasma discharge. The plasma-neutral collision frequency is the largest influencing factor in determining power transfer into the fluid. This investigation shows that the RFGD microthruster concept can potentially provide thrust in the millinewton range while meeting stringent power/size limitations and achieving improvements in specific impulse, comparable with that of typical cold-gas thrusters.

Acknowledgments

The authors would like to thank J. P. Verboncoeur, C. K. Birdsall, and the Berkeley Plasma Theory and Simulation Group for the use of their XPDC1 code and providing assistance. We would also like to thank Mikhail Shneider for extremely valuable discussions of radio-frequency discharge physics. The computations reported in this paper were performed on a 16-CPU SunFire 4600, awarded through Sun Microsystems, Inc. Academic Excellence grant award EDUD-7824-070336-US.

References

[1] Sultan, C., Seereram, S., and Mehra, R., "Deep Space Formation Flying Spacecraft Path Planning," *International Journal of Robotics Research*, Vol. 26, No. 4, 2007, pp. 405–430. doi:10.1177/0278364907076709

[2] Choueiri, E., "A Critical History of Electric Propulsion: The First 50 Years (1906–1956)," *Journal of Propulsion and Power*, Vol. 20, No. 2, 2004, pp. 193–203. doi:10.2514/1.9245

[3] Pollard, J., and Martinez, M., "Spacecraft Electric Propulsion: An Overview," *Journal of Propulsion and Power*, Vol. 14, No. 5, 1998, pp. 688–699.

[4] Myers, R., "Overview of Major, U. S. Industrial Electric Propulsion Programs," 40th AIAA Joint Propulsion Conference and Exhibit, AIAA Paper 2004-3331, 2004.

[5] Wirz, R., Gale, M., Mueller, J., and Marrese, C., "Miniature Ion Thrusters for Precision Formation Flying," 40th AIAA Joint Propulsion Conference, AIAA Paper 2004-4115, July 2004.

[6] Warner, N., and Martinez-Sanchez, M., "Design and Preliminary Testing of a Miniaturized TAL Hall Thruster," 42nd AIAA Joint Propulsion Conference, AIAA Paper 2006-4994, July 2006.

[7] Tajmar, M., Genovese, A., and Steiger, W., "Indium Field Emission Electric Propulsion Microthruster Experimental Characterization," *Journal of Propulsion and Power*, Vol. 20, No. 2, 2004, pp. 211–218. doi:10.2514/1.9247

[8] Gamero-Castano, M., Hruby, V., Spence, D., Demmons, N., McCormick, R., and Gasdaska, C., "Micro- Newton Colloid Thruster for ST7-DRS Mission," 39th AIAA Joint Propulsion Conference, AIAA Paper 2003-4543, July 2003.

[9] Rayburn, C., Campbell, M., and Mattick, A., "Pulsed Plasma Thruster System for Microsatellites," *Journal of Spacecraft and Rockets*, Vol. 42, No. 1, 2005, pp. 161–170. doi:10.2514/1.15422

[10] Au, M., Schein, J., Gerhan, A., Wilson, K., Tang, B., and Krishnan, M., "Magnetically Enhanced Vacuum Arc Thruster (MVAT)," 40th AIAA Joint Propulsion Conference, AIAA Paper 2004-3618, July 2004.

[11] Chianese, S., and Micci, M., "Microwave Electrothermal Thruster Chamber Temperature Measurements and Performance Calculations," *Journal of Propulsion and Power*, Vol. 22, No. 1, 2006, pp. 31–37. doi:10.2514/1.15337

[12] Ketsdever, A. D., Wadsworth, D. C., and Muntz, E., "Predicted Performance and Systems Analysis of the Free Molecule Micro-Resistojet," *Micropropulsion for Small Spacecraft*, edited by M. Miccio, and A. Ketsdever, Progress in Astronautics and Aeronautics, Vol. 187, AIAA, Reston, VA, 2000, pp. 167–183.

[13] Hitt, D. L., Zakrzwski, C. M., and Thomas, M. A., "MEMS-based Satellite Micropropulsion via Catalyzed Hydrogen Peroxide Decomposition," *Smart Materials and Structures*, Vol. 10, 2001, pp. 1163–1175. doi:10.1088/0964-1726/10/6/305

[14] London, A., Ayon, A., Epstein, A., Spearing, S., Harrison, T., Peles, Y., and Kerrebrock, J., "Micro-Fabrication of a High Pressure Bipropellant Rocket Engine," *Sensors and Actuators A (Physical)*, Vol. 92, 2001, pp. 351–357. doi:10.1016/S0924-4247(01)00571-4

[15] Ziemer, J. K., and Merkowitz, S. M., "Microthrust Propulsion for the LISA Mission," AIAA Paper 2004-3439, 2004.

[16] Mueller, J., "Thruster Options for Microspacecraft: A Review and Evaluation of State-of-the-Art and Emerging Technologies," *Micropropulsion for Small Spacecraft*, edited by M. Miccio, and A. Ketsdever, Progress in Astronautics and Aeronautics, Vol. 187, AIAA, Reston, VA, 2000, pp. 45–137.

[17] Mueller, J., Pyle, D., Chakraborty, I., Ruiz, R., Tang, W., and Lawton, R., "Microfabricated Ion Accelerator Grid Design Issues: Electric Breakdown Characteristics of Silicon Dioxide Insulator Material," 34th AIAA Joint Propulsion Conference, AIAA Paper 98-3923, 1998.

[18] Messerole, J., "Erosion Resistance of Carbon-Carbon Ion Optics," *Journal of Propulsion and Power*, Vol. 17, No. 1, 2001, pp. 12–18.

[19] Marcuccio, S., Genovese, A., and Andrenucci, M., "FEEP Microthruster Technology Status and Potential Applications," 48th International Astronautical Federation Congress, International Astronautical Federation Paper 97-S.3.04, 1997.

[20] Lieberman, M., and Lichtenberg, A., *Principles of Plasma Discharges and Materials Processing*, 2nd ed., Wiley, New York, 2005.

[21] Raizer, Y., Shneider, M., and Yatsenko, N., *Radio Frequency Capacitive Discharges*, CRC Press, Boca Raton, FL, 1995.

[22] White, P. S., Best, S., Hrbud, I., Hartsfield, R., and Rose, M., "RF Plasma Thruster for SmallSat Applications," 35th AIAA Joint Propulsion Conference, AIAA 1999-2438, 1999.

[23] Alves, M., Lieberman, M., Vahedi, V., and Birdsall, C., "Sheath Voltage Ratio for Asymmetric RF Discharge," *Journal of Applied Physics*, Vol. 69, No. 7, 1991, pp. 3823–3829. doi:10.1063/1.348436

[24] Raizer, Y., *Gas Discharge Physics*, Springer–Verlag, New York, 1991.

[25] Leiter, H., and Feili, D., "RIT 15S- A Radio Frequency Ion Engine for High Specific Impulse Operation," 37th AIAA Joint Propulsion Conference, AIAA Paper 2001-3491, July 2001.

[26] Pollard, J., Lichtin, D., and Cohen, R., "RF Discharge Electrothermal Propulsion: Results from a Lab-Scale Thruster," 23rd AIAA Joint Propulsion Conference, AIAA Paper 1987-2124, 1987.

[27] Groh, K., and Loeb, H. W., "State-of-the-Art of Radio Frequency Ion Thrusters," *Journal of Propulsion and Power*, Vol. 7, No. 4, 1991, pp. 573-579.

[28] Brewer, L., Karras, T., and Grahm, D., "Preliminary Results of a High Power RF Thruster Test," 25th AIAA Joint Propulsion Conference, AIAA Paper 1989-2382, 1989.

[29] Olson, L., "Operation of a 50 W Radio Frequency Plasma Thruster," 37th AIAA Joint Propulsion Conference, AIAA Paper 2001-3903, 2001.

[30] Olson, L., "A More Efficient Radio Frequency Plasma Thruster," 35th AIAA Joint Propulsion Conference, AIAA Paper 1999-2437, 1999.

[31] Mironer, A., and Hushfar, F., "Radio Frequency Heating of a Dense Moving Plasma," *AIAA Electric Propulsion Conference*, AIAA, New York, Mar. 1963, pp. 63045-63.

[32] Moravej, M., Yang, X., Nowling, G., Change, J., and Hicks, R., "Physics of High-Pressure Helium and Argon Radio-Frequency Plasmas," *Journal of Applied Physics*, Vol. 96, No. 12, 2004, pp. 7011–7017. doi:10.1063/1.1815047

[33] Sommerer, T., Hitchon, W., and Lawler, J., "Electron Heating Mechanisms in Helium RF Glow Discharges: A Self-Consistent Kinetic Calculation," *Physical Review Letters*, Vol. 63, No. 21, 1989, pp. 2361–2364. doi:10.1103/PhysRevLett.63.2361

[34] Novikova, T., Kalache, B., and Bulkin, P., "Numerical Modeling of Capacitively Coupled Hydrogen Plasmas: Effects of Frequency and Pressure," *Journal of Applied Physics*, Vol. 93, No. 6, 2003, pp. 3198–3206. doi:10.1063/1.1555678

[35] Okhrimovskyy, A., Bogaerts, A., and Gijbeis, R., "Incorporating the Gas Flow in a Numerical Model of RF Discharges in Methane," *Journal of Applied Physics*, Vol. 96, No. 6, 2004, pp. 3070–3076. doi:10.1063/1.1782951

[36] Moravej, M., Yang, X., and Hicks, R., "A Radio-Frequency Nonequilibrium Atmospheric Pressure Plasma Operating with Argon and Oxygen," *Journal of Applied Physics*, Vol. 99, May 2006, Paper 093305. doi:10.1063/1.2193647

[37] Yuan, X., and Raja, L., "Computational Study of Capacitively Coupled High-Pressure Glow Discharges in Helium," *IEEE Transactions on Plasma Science*, Vol. 31, No. 4, 2003, pp. 495–503. doi:10.1109/TPS.2003.815479

[38] White, P., "Preliminary Investigation of an RF Plasma Thruster," M.S. Thesis, Auburn Univ., Auburn, AL, 1999.

[39] Birdsall, C., "Particle-in-Cell Charged-Particle Simulations Plus Monte Carlo Collisions With Neutral Atoms, PIC-MCC," *IEEE*

Transactions on Plasma Science, Vol. 19, No. 2, Apr. 1991, pp. 65–85. doi:10.1109/27.106800

[40] Lawson, W., "Particle Simulation of Bounded 1D Plasma Systems," *Journal of Computational Physics*, Vol. 80, No. 2, 1989, pp. 253–276. doi:10.1016/0021-9991(89)90099-5

[41] Schweigert, I., and Schweigert, V., "Combined PIC-MCC Approach for Fast Simulation of a Radio-Frequency Discharge at a Low Gas Pressure," *Plasma Sources Science and Technology* , Vol. 13, Apr. 2004, pp. 315–320. doi:10.1088/0963-0252/13/2/018

[42] Lawler, J., and Kortshagen, U., "Self-Consistent Monte Carlo Simulations of the Positive Column of Gas Discharges," *Journal of Physics D: Applied Physics*, Vol. 32, Oct. 1999, pp. 3188–3198. doi:10.1088/0022-3727/32/24/315

[43] Raizer, Y. P., and Shneider, M., "Coaxial Medium-Pressure RF Discharge: Dynamics of Plasma Oscillations," *Plasma Physics Reports*, Vol. 21, No. 3, 1995, pp. 260–267.

[44] Ivanov, M., Kashkovsky, A., Gimelshein, S., Markelov, G., Alexeenko, A., Bondar, Y., Zhukova, G., Nikiforov, S., and Vaschenkov, P., "SMILE System for 2D/3D DSMC Computations," *Proceedings of the 25th International Symposium on Rarefied Gas Dynamics*, House of SBRAS, Novosibirsk, Russia, 2006, pp. 539–544.

[45] Alexeenko, A., Gimelshein, S., Levin, D., Ketsdever, A. D., and Ivanov, M., "Measurements and Simulation of Orifice Flow for Micropropulsion Testing," *Journal of Propulsion and Power*, Vol. 19, No. 4, 2003, pp. 588–594.

[46] Shneider, M., Zhang, Z., and Miles, R., "Plasma Induced by Resonance Enhanced Multiphoton Ionization in Inert Gas," *Journal of Applied Physics*, Vol. 102, No. 12, 2007, Paper 123103. doi:10.1063/1.2825041

[47] Stein, W., Alexeenko, A., and Hrbud, I., "Performance Modeling of an RF Coaxial Plasma Thruster," 43rd AIAA Joint Propulsion Conference, AIAA Paper 2007-5292, 2007.

[48] Ketsdever, A., Clarbough, M., Gimelshein, S., and Alexeenko, A., "Experimental and Numerical Determination of Micropropulsion Device Efficiencies at Low Reynolds Numbers," *AIAA Journal*, Vol. 43, No. 3, 2005, pp. 633-641. doi:10.2514/1.10284

G. Spanjers
Associate Editor